International Journal of Biological Macromolecules 258 (2024) 128969

Contents lists available at ScienceDirect

International Journal of Biological Macromolecules

journal homepage: www.elsevier.com/locate/ijbiomac

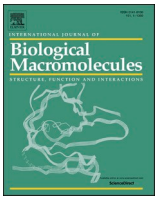

Overlapping characteristics of weak interactions of two transcriptional regulators with WDR5

Mohammad Ahmad [a,1], Ali Imran [a,1], Liviu Movileanu [a,b,c,*]

[a] Department of Physics, Syracuse University, 201 Physics Building, Syracuse, NY 13244-1130, USA
[b] Department of Biomedical and Chemical Engineering, Syracuse University, 329 Link Hall, Syracuse, NY 13244, USA
[c] The BioInspired Institute, Syracuse University, Syracuse, NY 13244, USA

ARTICLE INFO

Keywords:
Protein-protein interactions
Fluorescence resonance energy transfer
Biolayer interferometry

ABSTRACT

The WD40 repeat protein 5 (WDR5) is a nuclear hub that critically influences gene expression by interacting with transcriptional regulators. Utilizing the WDR5 binding motif (WBM) site, WDR5 interacts with the myelocytomatosis (MYC), an oncoprotein transcription factor, and the retinoblastoma-binding protein 5 (RbBP5), a scaffolding element of an epigenetic complex. Given the clinical significance of these protein-protein interactions (PPIs), there is a pressing necessity for a quantitative assessment of these processes. Here, we use biolayer interferometry (BLI) to examine interactions of WDR5 with consensus peptide ligands of MYC and RbBP5. We found that both interactions exhibit relatively weak affinities arising from a fast dissociation process. Remarkably, live-cell imaging identified distinctive WDR5 localizations in the absence and presence of full-length binding partners. Although WDR5 tends to accumulate within nucleoli, WBM-mediated interactions with MYC and RbBP5 require their localization outside nucleoli. We utilize fluorescence resonance energy transfer (FRET) microscopy to confirm these weak interactions through a low FRET efficiency of the MYC-WDR5 and RbBP5-WDR5 complexes in living cells. In addition, we evaluate the impact of peptide and small-molecule inhibitors on these interactions. These outcomes form a fundamental basis for further developments to clarify the multitasking role of the WBM binding site of WDR5.

1. Introduction

The 334-residue WD40 repeat protein 5 (WDR5) is a highly conserved member of the human proteome ubiquitously expressed in all tissues [1]. WDR5 is a highly conserved protein among numerous organisms, suggesting its multiple roles [2]. Notably, all WDR5 proteins from vertebrates share at least 90 % of their sequence identity [3]. Remarkably, human and mouse WDR5 sequences are identical [4]. Spanning an extended evolutionary scale, WDR5 homologs of fruit fly and basal metazoa share 95 and 90 % identity to human WDR5, respectively, when the entire WD40-repeat region is considered [5–8]. This protein has emerged as a critical player in diverse cellular functions, especially in epigenetic regulation [9–15]. WDR5 is an integral component of the large, multi-subunit methyltransferase complexes of mixed lineage leukemia (MLL/SET1) that catalyze the methylation of histone H3 at lysine 4 (H3K4), a hallmark of gene activation [2,16]. Knockdown of WDR5 disrupts the MLL/SET1 complexes through their protein-protein interactions (PPIs). This way, the global methylation patterns of H3K4 are affected [17]. These alterations are linked to abnormal transcriptional programs that promote malignancy [18].

Beyond WDR5's role in histone modification, recent research has highlighted its participation in the cell cycle progression [4] and stem cell self-renewal [19,20]. WDR5 is also involved in the modulation of histone deacetylase (HDAC3) complex; thereby, this property adds another dimension to the multifaceted role of WDR5 in gene regulation [21,22]. It has also been discovered that WDR5 interacts with numerous ligands, including peptides [23–25], proteins [4,13,26], nucleic acids [27], and small molecules [28–30]. There is evidence that WDR5 plays a crucial role in fostering tumorigenesis across various cancers [31–34], showing its potential as a promising therapeutic target [6,26,35,36]. Hence, this is a multitasking protein hub with numerous regulatory roles in cellular processes [2,4,26]. Moreover, WDR5 features nongenomic activities, including different cell polarity, shape, and motility tasks [37,38].

* Corresponding author at: Department of Physics, Syracuse University, 201 Physics Building, Syracuse, NY 13244-1130, USA.
E-mail address: lmovilea@syr.edu (L. Movileanu).
[1] These authors contributed equally to this manuscript.

https://doi.org/10.1016/j.ijbiomac.2023.128969
Received 4 August 2023; Received in revised form 18 December 2023; Accepted 20 December 2023
Available online 27 December 2023

WDR5 performs various cellular functions by interacting with multiple proteins using its two evolutionarily conserved regions known as the WDR5 interaction (Win) [17,39–41] and WDR5 binding motif (WBM) [42] sites. The Win site, an extensively studied region, is nestled deeply within the cavity of WDR5 and binds to the N-terminal tail of histone H3 and MLL/SET1 family members of methyltransferases [39,43,44]. On the contrary, the WBM site is located on the surface of WDR5 and is distinguished by the presence of two hydrophobic pockets [45]. However, the kinetics and dynamics of this site have yet to be investigated in detail compared to the Win site, highlighting an urgent need for its thorough exploration and comprehensive understanding.

The WBM site mediates interactions with diverse binding partners, including MYC [45] and RbBP5 [42,46]. MYC is a highly influential oncoprotein transcription factor that regulates cell cycle progression, apoptosis, cellular transformation, and stem cell pluripotency. Aberrant MYC expression is linked to numerous human cancers [47], indicating its oncogenic potential [48]. Interaction of WDR5 with MYC facilitates a stronger binding of MYC to the chromatin [49]. RbBP5 is an integral part of the MLL/SET1 enzymatic complex [13]. For histone methylation, the RbBP5-WDR5 interaction is crucial for assembling the large MLL/SET1 enzymatic complex. The specificity of these interactions underscores the fine-tuned regulatory role that WDR5 plays in its complex network of PPIs.

Understanding the molecular basis of these WBM-facilitated interactions with MYC and RbBP5 is imperative for a better understanding of the functional roles of WDR5. In this work, we employed the biolayer interferometry (BLI) [50] to illuminate the kinetic fingerprint of these interactions. This approach reveals relatively weak affinities of the WBM site-enabled interactions compared to the Win site-mediated interactions [23], which resulted from a fast dissociation process. In addition, we have performed the live-cell imaging of HeLa cells using various WDR5, MYC, and RbBP5 fusion constructs to study the localization dynamics of these nuclear proteins. Colocalization analyses revealed that the presence of its binding partners significantly influences the nucleolar accumulation of WDR5. A live-cell FRET microscopy [51,52] was also employed to uncover the weak MYC-WDR5 and RbBP5-WDR5 interactions. Moreover, we performed the inhibitor assays to examine the potential of peptide and small-molecule inhibitors to disrupt these clinically relevant PPIs. Our findings provide a fundamental platform for future studies to disentangle the multiple functional tasks of WDR5 under physiological and disease-like conditions.

2. Experimental section

2.1. Computational prediction and molecular docking

The three-dimensional (3D) conformations of the full-length MYC and RbBP5 were predicted via AlphaFold2 [53–55]. The amino acid sequences of MYC and RbBP5 were obtained from Uniprot (MYC-P01106, RbBP5- Q15291). The parameters used for the 3D structure prediction were kept in the default [53,54]. These predicted structures were subsequently compared with the truncated versions of the published PDB structures to evaluate these folded domains. Molecular docking between MYC and WDR5, as well as between RbBP5 and WDR5, was performed using High Ambiguity Driven protein−protein Docking (HADDOCK) tool (v2.4) [56]. All parameters related to sampling, clustering, and distance restraint were maintained at their default settings, except the hydrogen bond cutoff, which was established at 4 Å.

2.2. Expression plasmids

The cDNA of WDR5 was cloned in the pmVenus-C1 (Addgene #27794, Watertown, MA) at *BglII* and *HindIII* sites and in the pmVenus-N1 (Addgene #27793) at *NheI* and *AgeI* sites. The MYC and its truncated variant MYC-T (residues 151–328), which included the nuclear localization sequence, were cloned in pmScarlet-I-C1 (Addgene #85044) at *BglII* and *HindIII* sites and in pLifeAct-mScarlet-I-N1 (Addgene #85054) at *NheI* and *BamHI* sites. In the latter, LifeAct was replaced by our targeted gene. The cDNA of RbBP5 was cloned in the pmScarlet-I-C1 at *BglII* and *HindIII* sites and in pLifeAct-mScarlet-I-N1 (Addgene #85054) at *NheI* and *BamHI* sites. All these cDNAs were genetically fused to the fluorescent proteins using a flexible glycine-serine-rich linker $(GSS)_2$. The cDNAs of PATagRFP and HaLoTag were amplified from pEGFR-PATagRFP (Addgene #31950) and pHalo5678Tag-PS (Addgene #86626). mVenus in pmVenus-N1-WDR5 was replaced by either PATagRFP or HaLoTag. The cDNAs of the proteins were amplified using a set of primers (Supplementary Table S1). pTagRFP-C1-Fibrillarin (Addgene #70649) was used to identify the nucleolar region in HeLa cells. pmScarlet-I-H2A (Addgene #85053) was utilized to visualize the H2A localization and its interaction with WDR5. DNA sequencing was used to validate all cloning and mutagenesis work (Genscript, Piscataway, NJ). Supplementary Fig. S1 shows the schematic illustrations of the constructs used in this study. The N-terminus truncated WDR5 ($WDR5^{23–334}$) cloned in pET3a vector, named pET3a-WDR5, was gifted by Michael Cosgrove. pmVenus-C1 (Addgene plasmid #27794) and pmVenus-N1(Addgene #27793) were gifted by Steven Vogel. pmScarlet-I-C1 (Addgene #85044), pLifeAct_mScarlet-I_N1 (Addgene #85054), and pmScarlet-I-H2A (Addgene #85053) were gifted by Dorus Gadella. pTagRFP-C1-Fibrillarin (Addgene #70649) was gifted by David Sabatini. pEGFR-PATagRFP was obtained from Vladislav Verkhusha (Addgene #31950). Thomas Leonard and Ivan Yudushkin gifted pHaloTag-PS (Addgene #86626).

2.3. Protein expression and purification

WDR5 was purified similarly as described previously [23]. Briefly, the pET3a vector containing the 6 × His-TEV-$WDR5^{23–334}$ sequence was transformed into Rosetta™ 2 BL21(DE3)pLysS (Novagen through Millipore-Sigma, Burlington, MA; Cat #71403) competent *E. coli* cells. Here, TEV is the cleavage site by the Tobacco Etch Virus (TEV). These cells were grown overnight on Luria-Bertani (LB) agar carbenicillin/chloramphenicol selection plates at 37 °C. A single colony from these transformations was used to inoculate 50 ml Terrific Broth (TB) starter culture media. These cells were grown overnight at 30 °C. On the next day, 1 l TB media were inoculated by the starter culture. These expression cultures were grown at 37 °C for 2.5 h and then left at room temperature for 30 min. Cells were induced with 100 μM isopropyl *β*-D-1-thiogalactopyranoside (IPTG). They were grown for 20 h at 16 °C. Pellets were harvested, and the lysis was achieved using a Model 110 L microfluidizer (Microfluidics, Newton, MA). The lysis buffer contained 300 mM KCl, 50 mM Tris-HCl, 1 mM phenylmethylsulfonyl fluoride (PMSF), EDTA-free protease inhibitor, and pH 7.5. The lysate was spun down. The supernatant was processed through a Ni-NTA column integrated with an NGC Quest 10 Plus Chromatography System (Bio-Rad, Hercules, CA). WDR5 was eluted using the buffer containing 500 mM imidazole, 300 mM KCl, 50 mM Tris-HCl, and pH 7.5. The 6 × His tag was cleaved using the TEV protease. The Ni-NTA column was again used to remove the 6 × His tag and TEV protease from protein samples. Pure fractions were pooled together and used for the BLI experiments.

2.4. Peptide synthesis, labeling, purification, and analysis

All label-free peptides and biotin-labeled peptides for BLI experiments were synthesized and purified by GenScript (Piscataway, NJ). These peptides were purified to at least 95 % purity. The peptides for BLI experiments were biotinylated at the N-terminus. The unlabeled peptides were acetylated at the N-terminus. All the peptides were amidated at the C-terminus. GenScript provided the purity confirmation, amino acid analysis, and solubility testing.

2.5. Biolayer interferometry (BLI)

BLI studies were conducted using an OctetRED384 platform at a sampling rate of 10 kHz (FortéBio, Fremont, CA). The assays were performed similarly in our previous studies [23]. In this assay, we used the truncated version of WDR5$^{23–334}$. For the sake of simplicity, we name this variant WDR5 throughout this article. As ligands, the N-terminal biotinylated peptides were immobilized onto streptavidin (SA)-coated BLI sensors (Sartorius, Bohemia, NY). A nine-residue Gly/Ser-rich peptide spacer was inserted between the biotinylated site and the targeted peptide sequence (e.g., MbIIIb and RP5) to prevent steric hindrance. This way, we generated a ~3 nm distance between the BLI sensor and peptide sequence. These sensors were dipped into analyte-containing wells to obtain sensorgrams corresponding association phases. Then, the sensors were placed in analyte-free wells to obtain sensorgrams corresponding to dissociation curves. Unless specified, most experiments' running buffer included 150 mM NaCl, 20 mM Tris-HCl, 1 mg/ml bovine serum albumin (BSA), 1 mM TCEP, and pH 7.5.

For salt analysis experiments, we used buffers that contained 20 mM Tris-HCl, 1 mM TCEP, and 1 mg/ml BSA. Here, the NaCl concentration, [NaCl], varied at 50, 150, 300, and 600 mM. For the inhibition experiments, an additional non-biotinylated WBM inhibitor peptide and small-molecule inhibitor, C12, was added to the analytes (6UOZ.pdb; Supplementary Fig. S2) [30]. Baseline sensorgrams of the reference wells were subtracted from binding curves for the corresponding analyte concentrations. No ligand was immobilized on the reference well's sensors, and reference sensors were dipped into the wells that contained only the analyte. The binding curves were analyzed and fitted using the Octet Data Analysis software (FortéBio). Global fitting, which was performed using several analyte concentrations, provided the apparent association (k_a) and dissociation (k_d) constants [23,24]. The equilibrium dissociation constant, K_D, was indirectly determined using the k_a and k_d values. Three distinct BLI measurements were executed for all inspected interactions.

2.6. Cell culture and transfection

Cells were cultured in collagen-coated or non-coated six-well plates (Cellvis, Mountain View, CA). The cell density was ~2 × 10^5 cells per well. Cells were kept in a 5%CO_2 and 70 % relative humidity environment at 37 °C. A PCR test was conducted to detect any potential mycoplasma contamination in the cultures. HeLa and HEK-293T cells were transfected using Fugene-HD (Promega, Madison, WI) or Lipofectamine 3000 (Invitrogen by Thermo Fischer Scientific, Carlsbad, CA) in serum-free Dulbecco's Modified Eagle Medium (DMEM). The transfection mixtures were prepared using Opti-MEM (Thermo Fisher Scientific) as the medium, along with a transfection reagent and a plasmid DNA. For co-transfection, a 1:1 ratio of donor and acceptor plasmids was used. To achieve a low expression and ensure comparable recombinant protein expression levels to endogenous WDR5, MYC, and RbBP5, a plasmid concentration ranging from ~500 to ~800 ng per well was utilized. Then, the transfection mixture was incubated at room temperature for 15–20 min before being transferred into the wells. After setting the transfection mixture with the cells for 5–6 h, complete media was added and allowed to express the recombinant proteins for ~one day. Cells were treated with Dulbecco's phosphate-buffered saline (DPBS) and replaced with imaging media (DMEM with 25 mM HEPES and no phenol red, Thermo Fisher Scientific).

2.7. Live-cell imaging

Live-cell imaging of HeLa cells expressing various constructs was performed using spinning-disc confocal microscopy (Yokogawa CSU-W1 50 μm 60 Pinhole) on an inverted Nikon Ti-E microscope with 60× water immersion objective (1.49 NA) in an incubation chamber (Okolab USA Inc., Ambridge, PA) and captured onto an Andor Zyla CMOS camera. Images were acquired using the NIS-Elements software. Time series data were saved as .nd2 files with metadata and analyzed using ImageJ/FIJI. Excitation lines for mVenus, a yellow fluorescent protein (YFP; 500 ms excitation), and mScarlet-I, a red fluorescent protein (RFP; 500 ms), were 488 and 561 nm, respectively. Lasers used for activation and excitation of PATagRFP were 405 nm and 561 nm, respectively. For HaLoTag imaging, cells were treated with Janelia Fluor X-554 (JFX-554) dye and incubated at 37 °C for 15 min. Then, cells were treated twice with DPBS, after which DPBS was exchanged with the imaging media. Images of HeLa cells co-expressing WDR5-mVenus + MYC-mScarlet-I or WDR5-mVenus + RbBP5-mScarlet-I were acquired for colocalization. Colocalization analysis was performed using the Coloc2 tool [57]. Here, we obtained an object-corrected Pearson coefficient by combining object-recognition-based colocalization analysis with pixel-intensity correlation.

2.8. Fluorescence resonance energy transfer (FRET) microscopy

Sensitized-emission FRET (seFRET) imaging was conducted by co-expressing the mVenus-tagged WDR5, and mScarlet-I tagged MYC (or RbBP5) at either the N or C terminus. For FRET imaging, images were acquired and processed as described previously [52]. Briefly, HeLa cells co-expressing these combinations were excited at 488 nm (500 ms excitation), and the emission was collected at 595 nm. The cells were transfected separately with the acceptor- and donor-only plasmids to measure the direct excitation of the acceptor at the donor excitation light (acceptor spectral bleed-through) and the emission of the donor into the FRET channel (donor spectral bleed-through), respectively. The donor and acceptor spectral bleed-through were corrected, and the FRET efficiency was normalized relative to the donor expression level. A low plasmid concentration was used to prevent bystander FRET [58]. Each image was assigned a pseudo color and underwent background removal. To calculate the normalized seFRET (NFRET) values, we followed the method developed by Xia and Liu (2001) [59] using the following equation:

$$\mathrm{NFRET} = \frac{I_{\mathrm{FRET}} - \alpha I_{\mathrm{mScarlet-I}} - \beta I_{\mathrm{mVenus}}}{\sqrt{I_{\mathrm{mScarlet-I}} I_{\mathrm{mVenus}}}} \quad (1)$$

$I_{\mathrm{mScarlet\text{-}I}}$ is the intensity of the acceptor. I_{mVenus} represents the intensity of the donor. I_{FRET} denoted the FRET intensity. α and β indicate the acceptor spectral bleed-through and the donor spectral bleed-through, respectively. NFRET was determined based on measurements obtained from three combinations of excitation and emission filters, namely (i) a donor-detection channel utilizing a donor-specific excitation and a donor-specific emission filter, (ii) a raw FRET channel employing a donor-specific excitation and an acceptor-specific emission filter, and (iii) an acceptor channel using an acceptor-specific excitation and an acceptor-specific emission filter.

2.9. Molecular graphics

PyMOL (v2.4.0 Schrödinger, LLC) was used for all protein representations.

3. Results and discussion

3.1. Computational analysis shows a substantial overlap between the binding sites of MYC and RbBP5 with WDR5

The crystal structure of WDR5 provides details of the WDR5 binding motif (WBM) binding site (Fig. 1a; PDB 2XL2) [42]. A cluster of several hydrophobic residues highlights this site [45]. To predict the three-dimensional conformations of the full-length MYC and RbBP5 proteins, we utilized AlphaFold2, an in-silico structure determination tool [53–55]. AlphaFold2 uses machine learning to model the three-dimensional structures of proteins based on their sequences. These

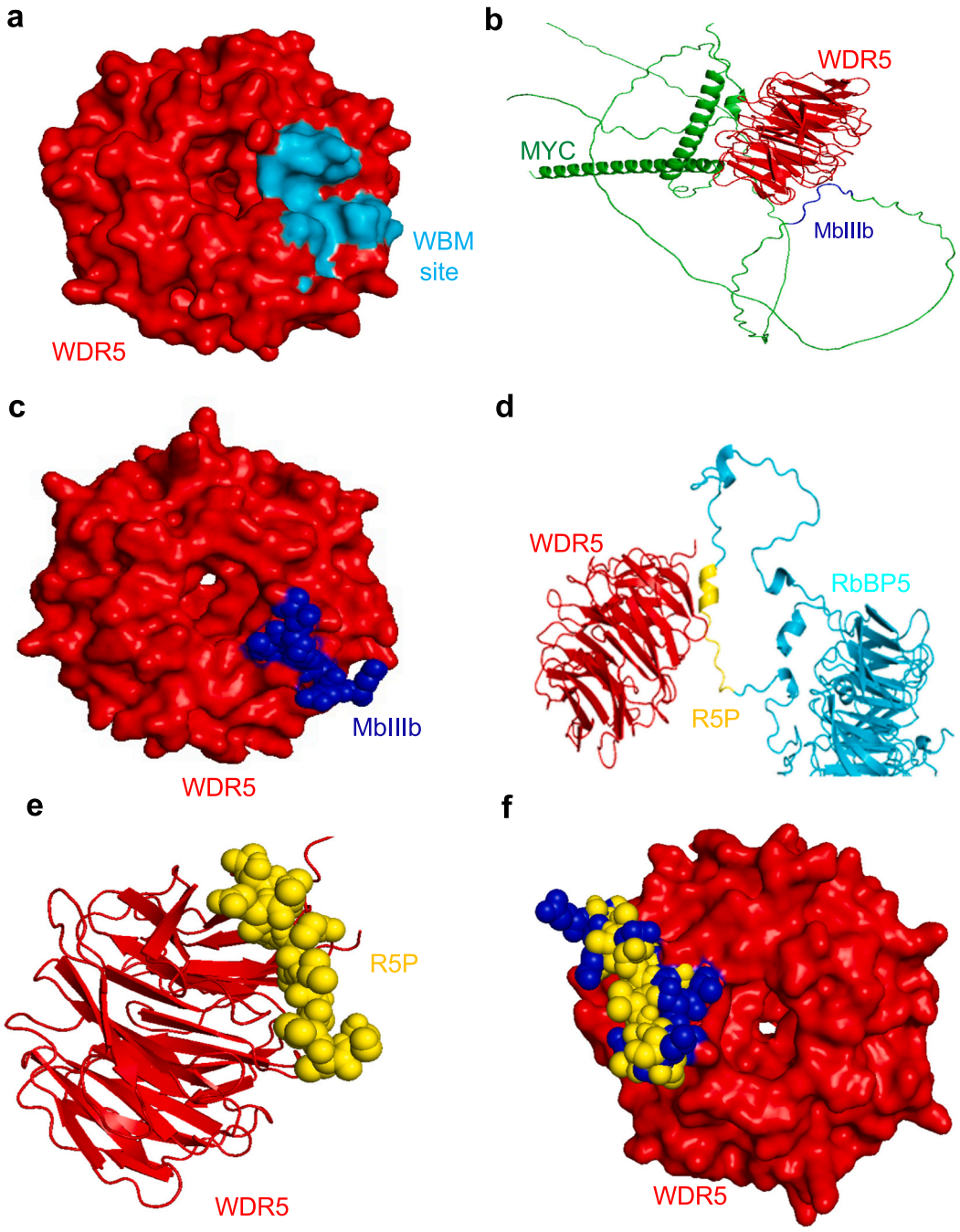

Fig. 1. Computational analysis of the MYC-WDR5 and RbBP5-WDR5 interactions.
(a) Surface view of WDR5 (red) showing the WBM site (cyan) (2XL2.pdb) [42]. (b) The interaction between the intrinsically disordered region of MYC (green) and WDR5 (red) was predicted using Haddock (V2.4.) [56]. The MYC binding region is illustrated in blue. The structure of MYC (green) was computed by AlphaFold2 [53–55], while WDR5 (red) was displayed using 2XL2.pdb [42]. For the sake of clarity, a limited representation of MYC is shown. (c) Surface view of WDR5 (red, surface) in complex with MbIIIb (blue, sphere) at the WBM site (4Y7R.pdb) [45]. (d) The interaction between RbBP5 (cyan) and WDR5 (red) was predicted using Haddock (V2.4.) [56]. The RbBP5 binding region is shown in yellow. The structure of RbBP5 (cyan) was predicted by AlphaFold2 [53–55], while WDR5 (red) was displayed using 2XL2.pdb [42]. For the sake of clarity, a limited representation of RbBP5 is shown. (e) WDR5 (red, ribbon) in complex with the R5P (yellow, sphere) at the WBM site (2XL2.pdb) [42]. (f) Superimposition of MbIIIb- and R5P-contacting surfaces on the WBM site of WDR5 using 4Y7R.pdb [45]and 2XL2.pdb [42], respectively. R5P (yellow) and MbIIIb (blue) are represented as spheres, and WDR5 is represented as a surface (red). Here, the superimposed surface view of WDR5 complexed with MbIIIb and R5P was rotated by 180° with respect to the top-view structures in (a) and (c). (b), (d), and (e) are tilted side-views of WDR5 to show its binding with MYC, RbBP5, and the R5P consensus peptide ligand, respectively.

predictions generate the five best protein structure models, the predicted Local Distance Difference Test (pLDDT) confidence scores per residue, and the predicted aligned error (PAE). Low pLDDTs and high PAEs indicate a disordered region of a specific protein. Except for the C-terminal helix-loop-helix motif, pLDDTs for most residues of MYC ranged between 25 and 70 (Supplementary Fig. S3a). Their corresponding PAEs were larger than 20 (Supplementary Fig. S3b). Computational predictions enabled the visualization of MYC's structured and disordered regions (Supplementary Fig. S3c), which correlated well with the magnitude of pLDDTs and PAEs.

Then, we conducted molecular docking of MYC and WDR5 using the High Ambiguity Driven protein−protein Docking (HADDOCK) tool (Experimental section) [56]. This exploration revealed the association between the disordered region of MYC (residues 259–267; Table 1) and the WBM site of WDR5 (Fig. 1b and c; Supplementary Fig. S4a) [45]. These residues are referred to as MbIIIb throughout this article. Three critical residues in the center of the MbIIIb, D263, V264, and V265, form noncovalent interactions with WDR5 (Supplementary Fig. S4b). This combination of MYC residues is also called the DVV triad. In the case of RbBP5, only the C-terminal domain showed low pLDDT confidence scores and high PAEs (Supplementary Fig. S5a–b). This forms an extended disordered region in the predicted RbBP5 protein (Supplementary Fig. S5c), like the reported PDB structure (Supplementary Fig. S5d; PDB 3KIW) [13]. The docking of RbBP5 and WDR5 displayed the binding interaction at the WDR5 outer surface (Fig. 1d; Supplementary Fig. S6), involving the conserved critical residues of RbBP5 between 369 and 381 (Fig. 1e; Table 1). These residues are referred to as RbBP5 Peptide (R5P). We conclude that the full-length MYC and RbBP5 proteins exhibit highly overlapping binding sites for a noncovalent interaction with WDR5 through its shallow hydrophobic WBM site (Fig. 1f).

3.2. Unraveling the kinetics of interactions mediated by the WBM site

The WBM site of WDR5 is an evolutionarily conserved region that facilitates interactions with various gene regulators. Their dysregulation affects physiological and disease-like conditions, including cancer [4]. We investigated the association (k_a) and dissociation (k_d) rate constants of the MbIIIb-WDR5 and R5P-WDR5 interactions using biolayer interferometry (BLI) measurements in a real-time setting [23,50]. This way, we wanted to compare the kinetics of WDR5 interactions with each of the competing peptide ligands MbIIIb and R5P against the WBM site. MbIIIb and R5P were immobilized onto the BLI sensor surface using a flexible $(GGS)_3$ peptide spacer and biotin-streptavidin chemistry [23]. At the same time, WDR5 was kept free in the well. This allowed for monitoring the association and dissociation phases of the peptide ligand-WDR5 complex by recording the changes in the interference pattern created by light reflected on the BLI sensor surface.

The association and dissociation phases of the MbIIIb-WDR5 interaction were noted by time-dependent increases and declines in the BLI signal responses, respectively (Fig. 2a; Supplementary Fig. S7). Baseline sensorgrams of the reference wells were subtracted from recorded binding curves for each WDR5 concentration (Supplementary Fig. S8). To acquire these baseline sensorgrams, ligand-free BLI sensors were dipped into wells containing WDR5 at various concentrations. Their relatively flat profiles and low BLI response levels indicate no significant nonspecific association of WDR5 with the sensor surface. The interaction between MbIIIb and WDR5 is predominantly driven by the hydrophobic and ionic forces produced by the critical DVV triad of residues (Supplementary Fig. S4b, Tables S2–S3). The WBM site of WDR5 encompasses a cluster of nonpolar residues (Y228, L240, L249, F266, V268, L288) [45]. The hydrophobic contacts mediating the MbIIIb -WDR5 interaction were intriguing and prompted us to investigate the impact of a point mutation within this triad. Hence, we tested the MbIIIb_V264G mutant and found a modest BLI response in the presence of WDR5 (Fig. 2b; Table 1), suggesting a significantly weaker MbIIIb_V264G-WDR5 interaction with respect to MbIIIb-WDR5. This outcome validates the specificity of our BLI experimental design for probing the MbIIIb-WDR5 interaction. Such a finding is in accordance with prior studies by Thomas and colleagues (2015) [45].

We also determined the association and dissociation phases for the R5P-WDR5 interaction (Fig. 2c; Supplementary Fig. S9). Because some BLI sensorgrams acquired at very high WDR5 concentrations showed a deviation from a single-exponential pattern, we called the k_a and k_d values the apparent kinetic constants of association and dissociation, respectively. Notably, the apparent association constants, k_a, of both peptide ligand-WDR5 complexes are similar. For example, the BLI-determined apparent k_a values for the MbIIIb-WDR5 and R5P-WDR5 interactions were $(9.0 \pm 1.3) \times 10^4$ and $(9.4 \pm 1.1) \times 10^4$ M^{-1} s^{-1}, respectively (Supplementary Table S4). The apparent dissociation rate constants, k_d, for the MbIIIb-WDR5 and R5P-WDR5 interactions, were $(8.3 \pm 1.5) \times 10^{-2}$ and $(14 \pm 1) \times 10^{-2}$ s^{-1}, respectively. The corresponding apparent K_D values of these interactions were (0.95 ± 0.27) μM and (1.5 ± 0.3) μM, respectively. Due to the high sequence similarity between R5P and MbIIIb within their binding site against WDR5, we postulated that a similar Val-to-Gly mutation in R5P would have a closely identical impact on the R5P-WDR5 interaction. In accordance with this expectation, no significant interaction was noted between R5P_V377G and WDR5 (Fig. 2d). Here, this mutation corresponds to Val-377 of RbBP5 (Table 1). Based on the sequence alignment between MbIIIb and R5P, we can comfortably say that the "DVT" sequence in R5P at positions 376–378 of RbBP5 is comparable to the "DVV" triad in MbIIIb at positions 263–265 of MYC.

This study demonstrates that BLI provides real-time binding kinetics data of biomolecular interactions, such as the apparent k_a and k_d. The equilibrium dissociation constant (K_D) may also be determined using this method in a steady-state equilibrium format [50]. However, it often needs more detailed information about the binding mechanism itself. Specifically, BLI does not provide insights into the binding interface that leads to the exact nature of biomolecular interactions [60,61]. It should be noted that the BLI sensorgrams collected at high analyte concentrations undergo a certain deviation from a single-exponential curve despite the subtraction of the reference from the binding curve (see above). The reason for this abnormal BLI response at high WDR5 concentrations is unclear, yet it remains to be elucidated in a future publication.

Table 1
The peptides used for this work and their sequences. The C-terminus of all peptides was amidated. The N-terminus of MbIIIb, R5P, and MbIIIb_V264G were biotinylated. The N-terminus of the WBM Inhibitor was acetylated. MbIIIb and R5P represent 259–267 and 369–381 residues of MYC and RbBP5, respectively. The binding residues of these peptides for WDR5 via the WBM site are marked in black. The N-terminal and C-terminal modifications are marked in blue, and the linkers are in green. Residues marked in red are Val-to-Gly amino acid mutations in the binding site of the consensus peptide ligands MbIIIb and RP5, which correspond to MYC and RbBP5 proteins, respectively.

Peptide name	Peptide sequence	Charge[a]
MbIIIb	$_{Biotinyl}$-GGSGGSGGSEEEIDVVSV-$_{NH2}$	−3.2
R5P	$_{Biotinyl}$-G G S G G S G G S A A E D E E V D V T S V D-$_{NH2}$	−5.3
MbIIIb_V264G	$_{Biotinyl}$-GGSGGSGGSEEEIDGVSVE-$_{NH2}$	−4.1
R5P_V377G	$_{Biotinyl}$-G G S G G S G G S A A E D E E V D G T S V D-$_{NH2}$	−5.2
WBM inhibitor	$_{Ac}$-A A E D E E V D V T S V D-$_{NH2}$	−5.2

[a] Charges of these peptides were calculated using protein calculator v3.4 by amino acid sequence at pH 7.5 (https://protcalc.sourceforge.net/). The amidation effect of the C terminus of these peptides was included in their charge calculations.

3.3. Salt dependence of the WBM-mediated the R5P-WDR5 interactions

Exploring the charge distribution of WDR5 reveals that the WBM site on the WDR5 surface displays a highly positive charge. At the same time, R5P exhibits a significant negative charge (Fig. 3a). Hence, it becomes evident that electrostatic effects might also play a substantial role in these peptide ligand-WDR5 interactions. We hypothesized that this interaction is sensitive to the shielding effects induced by salt. It is important to note that R5P was chosen for this study because it carries a greater negative charge than MbIIIb (Table 1). To test this hypothesis, we inferred the kinetics of these interactions in three additional buffers, maintaining similar concentrations of the solution constituents, such as Tris-HCl, TCEP, and BSA, while altering NaCl concentration, [NaCl], to 50 mM, 300 mM, and 600 mM, in addition to the previously tested of

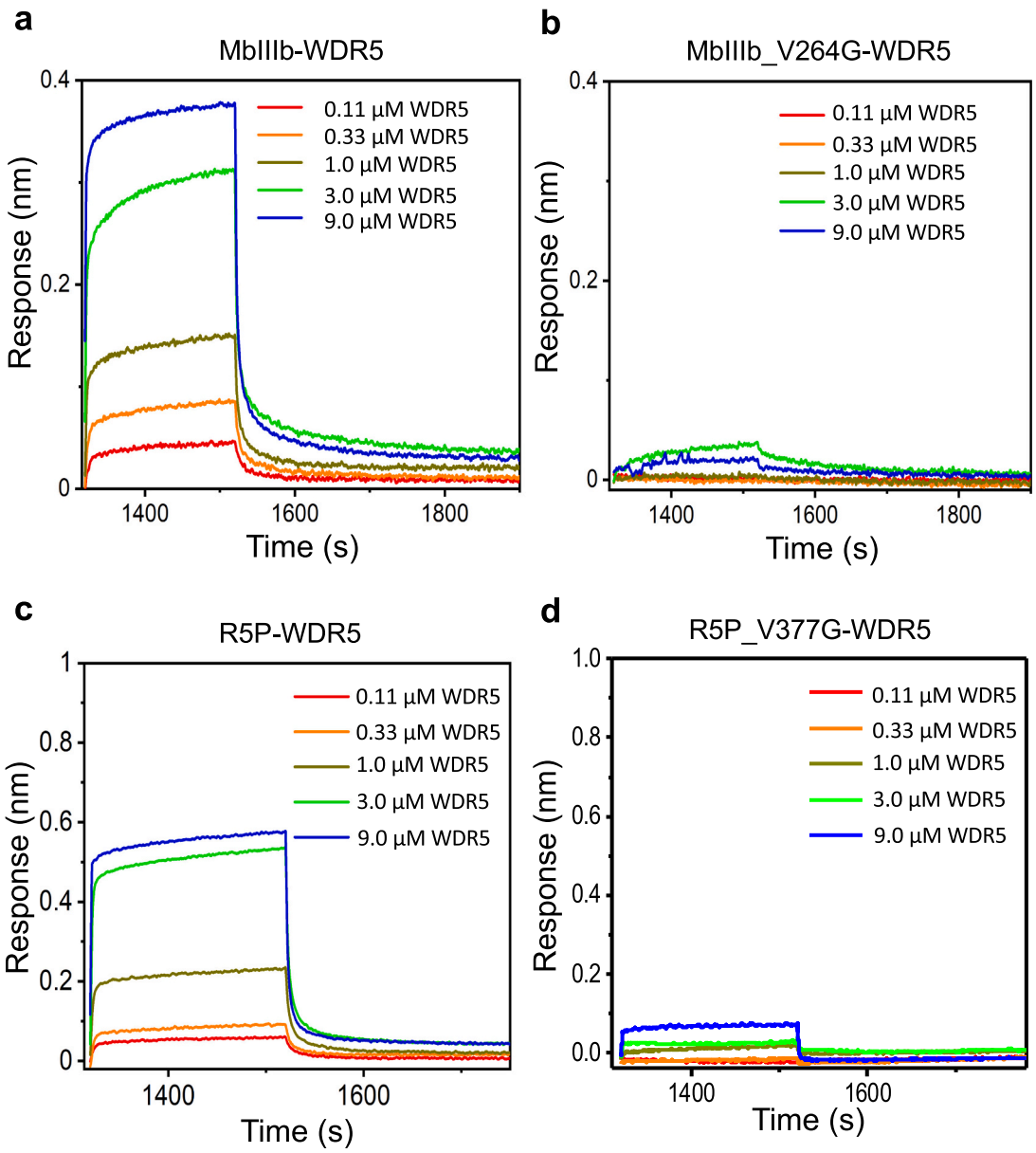

Fig. 2. Probing MbIIIb-WDR5 and R5P-WDR5 interactions using real-time biolayer interferometry (BLI). 5 nM biotin-tagged MbIIIb, MbIIIb_V264G or R5P was loaded onto streptavidin sensors for 10 min. WDR5 was injected as the analyte, and the corresponding association and dissociation curves were recorded. (a) This panel shows BLI sensorgrams obtained for the interaction of MbIIIb with WDR5. The sensors were dipped into wells containing different concentrations of WDR5, [WDR5]. (b) This panel presents BLI sensorgrams obtained for the interaction of MbIIIb_V264G with WDR5, as in panel (b). The sensors were dipped into wells containing different [WDR5] values. (c) This panel shows BLI sensorgrams obtained for the interaction of R5P with WDR5, as in (b). (d) This panel illustrates BLI sensorgrams acquired for the interaction of R5P_V377G with WDR5. The sensors were dipped into wells containing various [WDR5] values. Each sensorgram was recorded in at least three independent experiments.

150 mM NaCl (Fig. 2c). Our findings indicate that the change in the [NaCl] value substantially impacts the BLI response and binding kinetics (Fig. 3b–d; Supplementary Fig. S10 and Table S5). Furthermore, our approach facilitated the dissection of this effect in terms of alterations in the apparent association and dissociation rate constants. We observed a decrease in the apparent k_a at increased [NaCl] values (Fig. 4a). This was an expected outcome due to the reduced Debye screening length, effective interaction radius, and frequency of binding events [62]. Intriguingly, the [NaCl] value also influenced the apparent k_d. At 50 mM NaCl, the apparent k_d was much slower than at 600 mM NaCl (Fig. 4b). This observation accounts for the overall nonlinearity in the change of interaction strength in response to varying salt concentrations (Fig. 4c).

In addition, it should be noted that the maximal BLI response decreased by increasing [NaCl] from 50 to 600 mM. Again, this finding confirms the significantly declined binding activity at elevated salt concentrations monotonously. These experimental outcomes are in accordance with the general pattern of the salt dependence of the apparent kinetic and equilibrium determinations of protein-peptide and protein-protein interactions [62,63]. Another potential contribution to the salt-dependent change in the apparent binding kinetics and affinity is the modification of the secondary structure of R5P. This peptide is likely helical at physiological [NaCl] values, yet its structure may be altered by changing the salt concentration [53–55]. We conclude that the interplay between distinct ion-pair and hydrophobic interactions at the binding interface facilitates the formation of stable R5P-WDR5 complexes essential for their biological functions.

A summary of fit error analysis of the binding curves and error propagations corresponding to the MbIIIb-WDR5 and R5P-WDR5

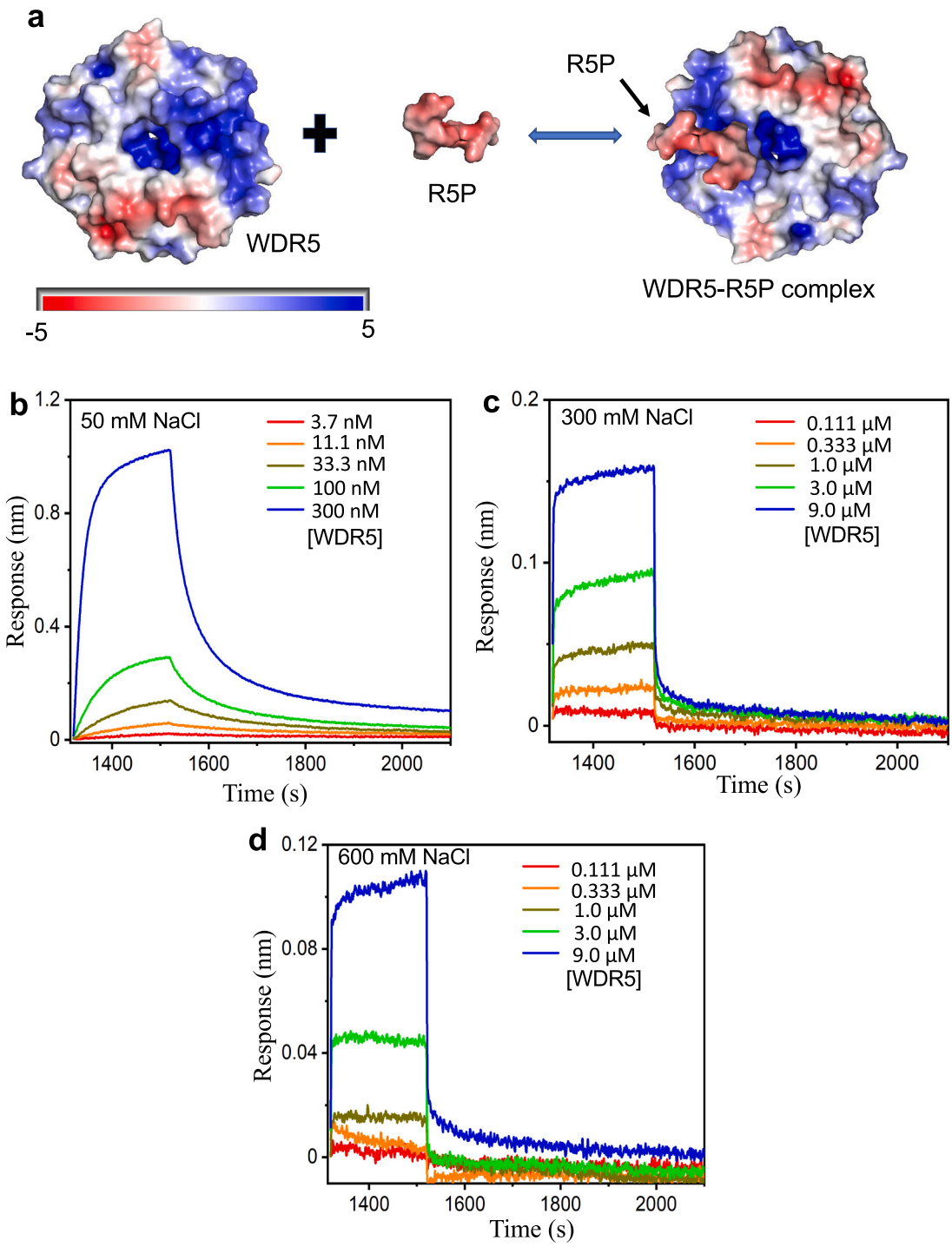

Fig. 3. Influence of salt on R5P's binding to WDR5. (a) Charge distribution on WDR5, R5P, and WDR5-R5P complex. (b) Sensorgrams were obtained for the R5P-WDR5 interaction at 50 mM NaCl. (c) The same as in (b), but at 300 mM NaCl. (d) The same as in (b), but at 600 mM NaCl. Each sensorgram was recorded in at least three independent experiments.

interactions is provided in the Supplementary Information file, Tables S6–S10. Again, BLI sensorgrams recorded under various salt conditions and at the highest WDR5 concentration show substantial deviations from the ideal 1:1 binding kinetics, declining the fit quality. In contrast, at lower WDR5 concentrations, the fit quality significantly improved, suggesting that more data acquisitions under these conditions are desirable for a better sensorgram fit. Despite these challenges, our affinity data align with prior measurements of the same interactions using different approaches. For example, using fluorescence polarization anisotropy, Tansey and co-workers reported a K_D of 9.3 μM for the MbIIIb-WDR5 interaction at 300 mM NaCl [45]. In comparison, our BLI-determined value was ~0.95 μM at 150 mM NaCl (Supplementary Table S4). Furthermore, isothermal titration calorimetry was previously utilized to obtain a K_D of 5.6 μM for the R5P-WDR5 interaction at 300 mM NaCl [42], which compares well with the BLI-determined value of 1.9 μM obtained in this study at the same salt concentration. These data demonstrate that we can still probe the overall behavior of these interactions despite the apparent shortcomings of the BLI approach.

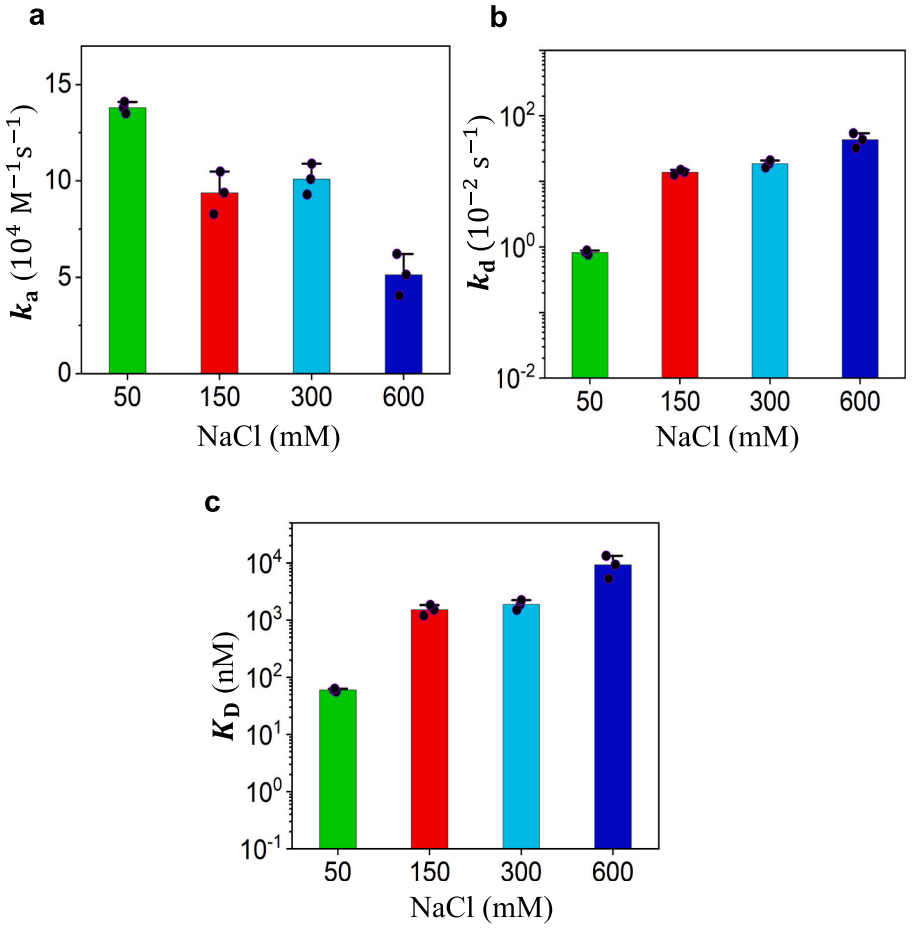

Fig. 4. Apparent kinetic and affinity constants of the R5P-WDR5 interaction at various salt concentrations. (a) The apparent association rate constants, k_a. (b) The apparent dissociation rate constants, k_d. (c) The apparent equilibrium dissociation constants, K_D. All the salt concentrations were repeated in three independent experiments. Each dot point shows one replicate. Data indicate mean ± s.d. using $n = 3$ independently executed experiments.

3.4. The analysis of the full-length WDR5, MYC, and RbBP5 subcellular localizations in living cells

Either mVenus or mScarlet-I was fused at the C terminus of WDR5, MYC, or RbBP5. We have created these fusion proteins to study their localizations and interaction patterns in living cells (Supplementary Fig. S1). mVenus is a monomeric yellow fluorescent protein (mYFP) exhibiting amplified photostability and enhanced brightness [64,65]. Furthermore, mScarlet-I is a very bright monomeric red fluorescent protein (mRFP) [66]. Surprisingly, while expressing WDR5-mVenus in HeLa cells, we discovered that WDR5 was localized within the nucleus but predominantly present in the nucleolar regions (Fig. 5a). To verify the nucleolar localization, we co-expressed WDR5-mVenus with TagRFP-Fibrillarin, a known nucleolar marker [67], and observed an elevated presence of WDR5 in the nucleolus, corroborating our initial findings (Fig. 5b). We also crosschecked the accumulation of WDR5 in HEK-293T cells expressing the WDR5-mVenus. Similar results as in HeLa cells were noted (Supplementary Fig. S11a).

We next assumed that the fluorescent protein used here could be the reason for the significant concentration of WDR5 in the nucleolus. To investigate this possibility further, we examined the WDR5 localization using alternative fluorescent proteins or synthetic dyes. For this purpose, we attached WDR5 to either HaLoTag [68], a tag labeled with JFX-554, or PATagRFP [69], a photoactivatable fluorescent protein. Following the expression of these fusion proteins, we conducted live-cell imaging and found that WDR5 accumulates in the nucleolus, regardless of the labeling strategy employed (Supplementary Fig. S11b–d). Subsequently, we explored the distribution patterns of WDR5's known binding partners, MYC [45,70] and RbBP5 [42], within HeLa cells. We fused MYC and RbBP5 with mScarlet-I and expressed them in HeLa cells. Our analysis showed that both proteins were exclusively localized within the nucleoplasm of these cells (Fig. 5c–f). Upon co-expression of WDR5 with MYC (Fig. 5g), we observed a nucleolar exclusion of WDR5 (Fig. 5h). We created a truncated version of MYC (MYC-T; residues 151–328) that contains the central region of MYC encompassing the MbIIIb binding domain. MYC-T showed the same effect of nucleolar exclusion of WDR5 (Fig. 5i–j). In these live-cell imaging experiments, while removing WDR5 from the nucleolus was noted in the presence of MYC or MYC-T, we cannot directly conclude that the short peptides utilized in BLI measurements would elicit the same effect.

A similar outcome was noted for the co-expression of RbBP5 and WDR5 (Fig. 5k–l), indicating that the presence of WDR5 in the nucleoli was primarily observed without its binding partners. This raises the possibility that WDR5 may possess an alternative function within the nucleolus, which could account for its prominent localization in this subnuclear compartment. We co-expressed WDR5 with the non-interacting histone H2A to validate this hypothesis and examined their subcellular localization. Our findings revealed that H2A did not interfere with WDR5's nucleolar localization (Supplementary Fig. S12), supporting the idea that WDR5 may exhibit a distinct function within the nucleolus without the binding partner. Colocalization analysis also showed a significant signal overlap between WDR5 and MYC and between WDR5 and RbBP5 (Supplementary Fig. S13). Fluorescence colocalization is frequently used to indicate that two molecules of interest are likely interacting partners. However, the complete colocalization of two proteins should be considered a piece of partial evidence

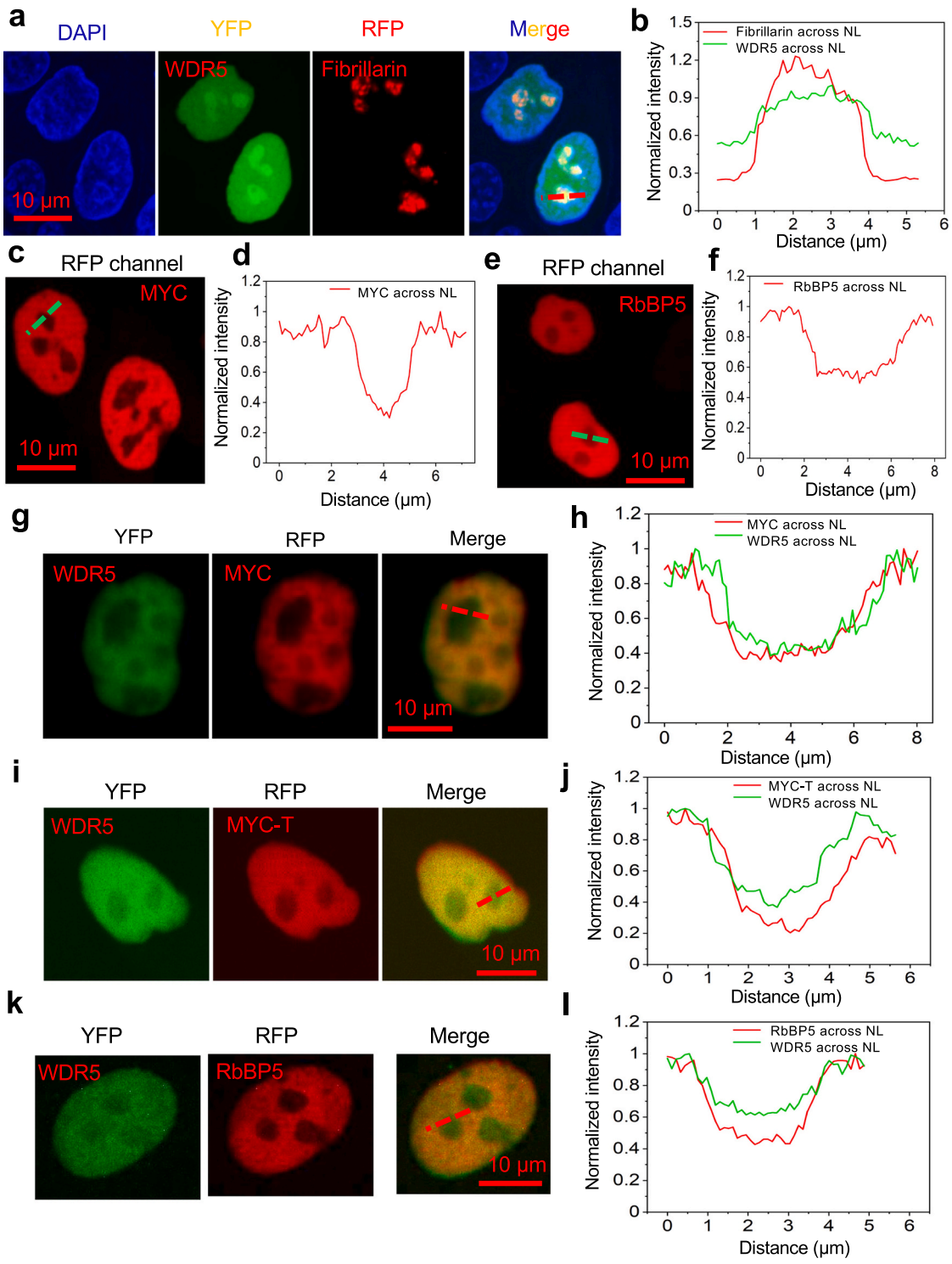

Fig. 5. Localization and colocalization analysis of WDR5, MYC, and RbBP5. (a) 5 μg/ml 4′,6-diamidino-2-phenylindole (DAPI) was used to visualize the nucleus. HeLa cells co-expressing WDR5-mVenus and mScarlet-I_Fibrillarin, and images were recorded at DAPI, YFP, and RFP channels, respectively. As shown in the merge channel, a line was placed as a region of interest across the nucleolus to check the distribution of WDR5 in HeLa cells. (b) The fluorescence intensity profile of WDR5 shows that WDR5 is hyperaccumulating in the nucleolus (NL), and the nucleolar marker protein, fibrillarin, confirmed it. (c) HeLa cells expressing MYC-mScarlet-I were recorded at the RFP channel. (d) Fluorescence intensity profile from (c). (e) mScarlet-I-RbBP5 at the RFP channel. (f) Fluorescence intensity profile from (e). (g) Hela cells co-expressing WDR5-mVenus and MYC-mScarlet-I. Images were recorded at YFP and RFP channels. An overlapping signal was observed, as indicated in the merged image. (h) The intensity profile shows that WDR5 and MYC are localized to the nucleoplasm in co-expressing cells (i) Colocalization of WDR5 and MYC-T. Images were recorded at YFP and RFP channels. An overlapping signal was observed, as indicated in the merged image. (j) Intensity profile shows that WDR5 and MYC-T are localized to the nucleoplasm in co-expressing cells. (k) Colocalization of WDR5 and RbBP5. Images were recorded at YFP and RFP channels. An overlapping signal was observed, as indicated in the merged image. (l) Intensity profile illustrates that the WDR5 and RbBP5 are localized to the nucleoplasm in coexpressing cells. For the analysis of fluorescence intensity curves, the number of cells (*n*) selected in the case of (b), (d), (f), (h), (i), and (l) were 29, 17, 19, 16, 13, and 23, respectively, from four independent experiments with similar results. In each curve, the fluorescence intensity was normalized to the maximum value. The dashed lines on microscopy images indicate the region of interest and correspond to the fluorescence intensity curves on the right side.

for their molecular interactions, as this necessitates further confirmatory approaches.

3.5. Live-cell FRET microscopy to visualize the WDR5-MYC and WDR5-RbBP5 interactions

The biophysical process of sensitized-emission fluorescence resonance energy transfer (seFRET) is suited for assessing physical macromolecular associations [51]. seFRET generates a detectable signal within the proximity of closely positioned chemically attached or genetically engineered fluorophores within the two macromolecules. During the FRET measurement, various factors can contaminate the seFRET signal. One possibility is that the acceptor is excited by the donor excitation. This contaminating factor is named the acceptor spectral bleed-through (ASBT, α). The other possibility is that the donor emission overlaps, at least partly, with the acceptor emission. This contaminating factor is also called the donor spectral bleed-through (DSBT, β). To evaluate these factors, we examined HeLa cells expressing either the donor or the acceptor fusion proteins (Supplementary Fig. S1). The normalized FRET (NFRET) was derived from the raw seFRET signal by

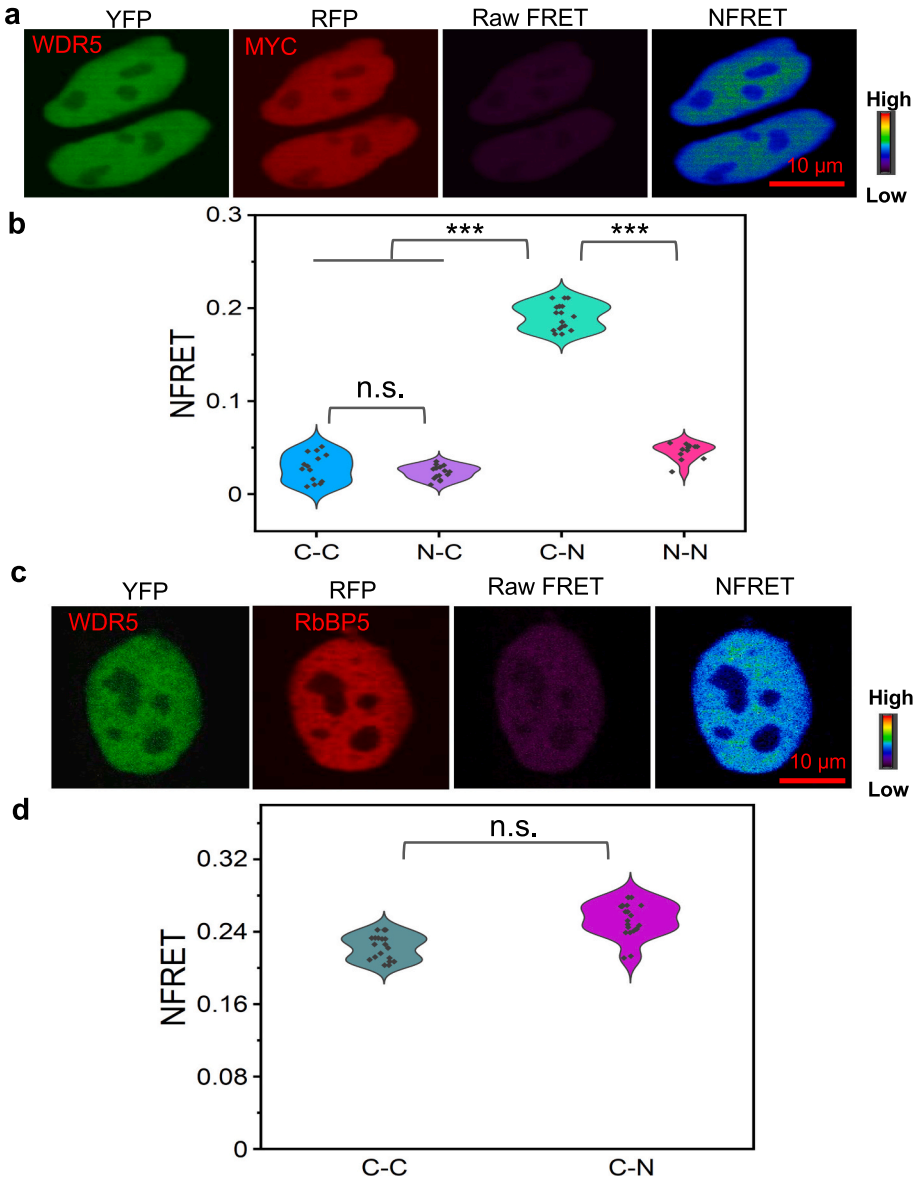

Fig. 6. Live-cell FRET imaging for detecting MYC-WDR5 and RbBP5-WDR5 interactions. Images of the HeLa cells were acquired at three detection channels (YFP, raw FRET, and RFP). The NFRET image was processed after subtracting the spectral bleed-through from the raw FRET signal. (a) FRET microscopy images of HeLa cells co-expressing WDR5-mVenus and mScarlet-I-MYC. The vertical color bar ranges from 0 to 0.5. (b) Violin plot showing the NFRET values for the WDR5 and MYC co-expressing cells with various fusion types. C—C represents mVenus and mScarlet-I fused at the C-terminus of WDR5 and MYC, respectively ($n = 14$). N—C means mVenus fused at the N-terminus of WDR5 and mScarlet-I fused at the C-terminus of MYC, respectively ($n = 16$). C—N represents mVenus fused at the C-terminus of WDR5 and mScarlet-I fused at the N-terminus of MYC, respectively ($n = 19$). N—N means mVenus and mScarlet-I fused at the N-terminus of WDR5 and MYC, respectively ($n = 12$). An unpaired two-tailed student *t*-test was utilized for a direct comparison. Statistical significance was considered at a test level $p < 0.05$ [73]. (c) FRET microscopy images of HeLa cells co-expressing WDR5-mVenus + mScarlet-I-RbBP5. (d) NFRET values for HeLa cells co-expressing WDR5 and RbBP5 with two fusion types. C—C represents mVenus and mScarlet-I fused at the C-terminus of WDR5 and RbBP5, respectively ($n = 19$). C—N represents mVenus fused at the C-terminus of WDR5 and mScarlet-I fused at the N-terminus of RbBP5, respectively ($n = 22$). The vertical color bar ranges from 0 to 0.5. Data in (b) and (d) show mean ± s.d. using three independent transfections. The reported NFRET values are recorded from the nucleoplasmic region. In (a) and (c), the horizontal scale bar is 10 μm. An unpaired two-tailed student t-test was utilized for a direct comparison. Statistical significance was considered at a test level $p < 0.05$ [73].

subtracting ASBT and DSBT. In a previous study, we thoroughly characterized the negative and positive FRET control constructs in HeLa cells utilizing mVenus (donor) and mScarlet-I (acceptor) fluorescent proteins [52]. The negative and positive FRET controls of this pair of fluorophores in living cells show an NFRET value of ~0.05 and ~0.44, respectively.

Fluorescence images of HeLa cells co-expressing WDR5-mVenus and mScarlet-I-MYC were captured and subsequently analyzed across multiple channels (Fig. 6a). A modest NFRET value was detected in cells co-expressing WDR5-mVenus and mScarlet-I-MYC with respect to that of corresponding positive FRET control, suggesting a moderate level of the interaction (Fig. 6b, Supplementary Table S11). The observed NFRET signal in these imaging experiments in living cells was significantly higher than the negative NFRET control values of the same pair of genetically engineered fluorophores [52]. This finding indicates the true interaction between the two labeled proteins. In contrast, no significant

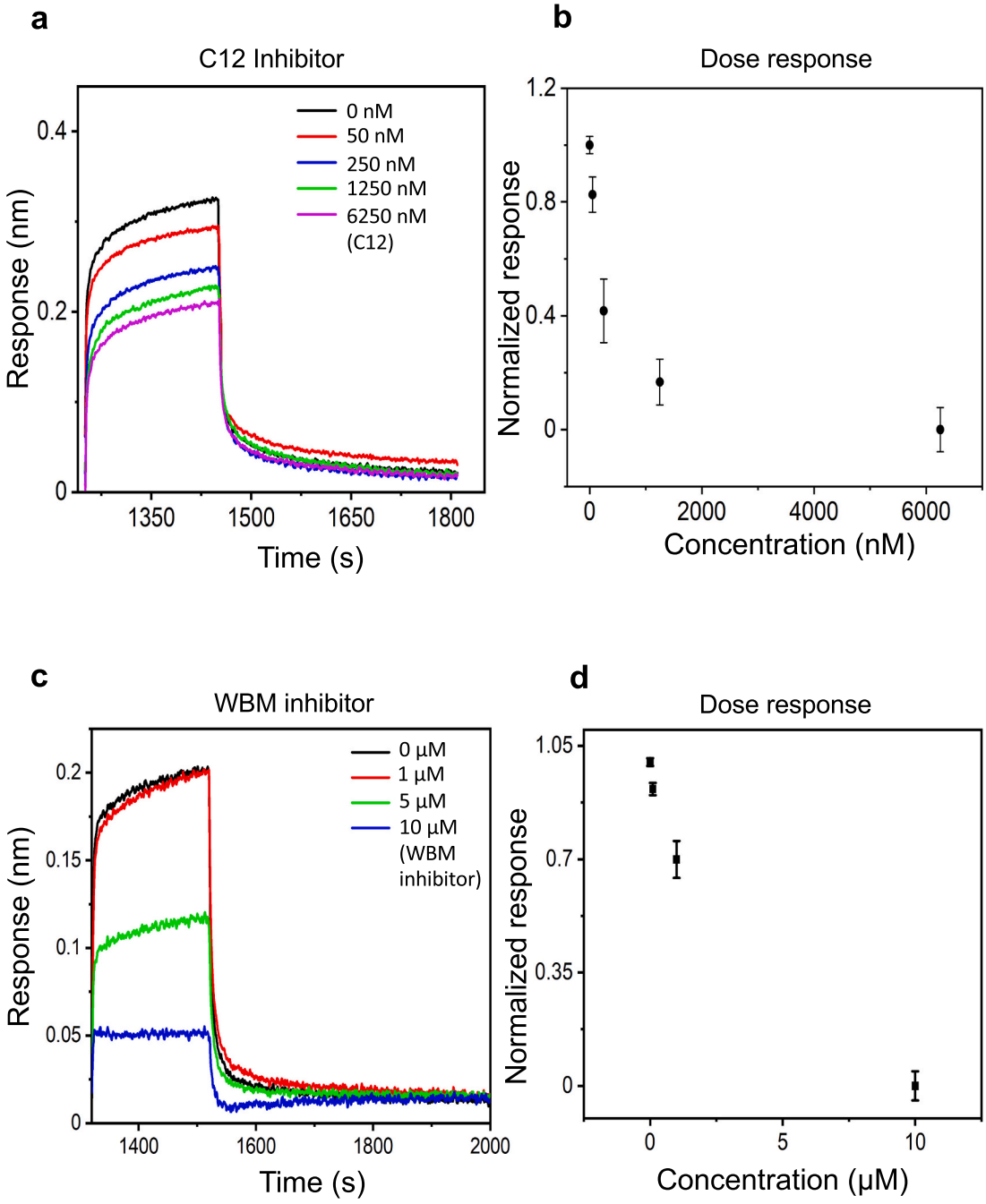

Fig. 7. Competitive inhibition of the MbIIIb-WDR5 and R5P-WDR5 interactions.
(a) The MbIIIb-WDR5 complex was inhibited with different concentrations of C12 inhibitor. Biotinylated MbIIIb was immobilized onto SA sensors (Experimental section). 3 µM WDR5-containing wells were spiked with different concentrations of C12 inhibitor. (b) The normalized responses were obtained with a C12 inhibitor to inhibit the MbIIIb-WDR5 interaction. (c) The R5P-WDR5 complex was inhibited with different concentrations of WBM inhibitor (non-biotinylated RbBP5 peptide). Biotinylated R5P was immobilized onto SA sensors (Experimental section). 3 µM WDR5-containing wells were spiked with different concentrations of WBM inhibitor. (d) Normalized responses were obtained for the inhibition of R5P-WDR5 interaction. In (b) and (d), the normalization BLI response was determined as $(R - R_{min})/(R_{max} - R_{min})$. Here, R is the BLI response at a given inhibitor concentration. R_{max} and R_{min} mean the maximum and minimum BLI responses determined for the inhibitor concentrations used in this study, respectively. Each data point shows mean ± s.d. using three independent experimental determinations.

variations in NFRET values were observed when employing alternative labeling configurations (Fig. 6b). One possible explanation for this observation is that the donor and acceptor fluorophores were not optimally positioned and oriented in proximity, which is a critical requirement for the FRET signal. In addition, images of HeLa cells co-expressing WDR5-mVenus + mScarlet-I-RbBP5 were analyzed (Fig. 6c). Slightly higher NFRET values were observed in these cells (Fig. 6d; Supplementary Table S11) compared to WDR5 and MYC co-expressing cells under the same labeling configuration.

FRET microscopy is a powerful and widely adopted technique in molecular biophysics and cellular biology to explore biopolymers' molecular interactions and conformational dynamics. However, the FRET signal depends on the distance between the two fluorophores. This article demonstrates that extensive genetic engineering is necessary until optimized proximity positions of the two fluorophores are determined for further examinations of the inter- or intra-molecular interactions. In this case, only the pair formed by WDR5-mVenus and mScarlet-I-MYC, namely the C-N configuration of the fluorophores, was efficient for probing the FRET signal (Fig. 6a–b). This result reinforces that FRET may not be suitable for studying interactions or conformational changes monitored by fluorophores at distant locations, a persistent limitation of this imaging modality in living cells. In addition to these challenges, FRET is highly sensitive to the local environmental factors of the fluorophores, such as pH, temperature, and ionic strength [51].

3.6. Assessing the effect of peptide and small-molecule inhibitors on the WBM site

MYC represents a challenging target for drug development due to its complex regulatory mechanisms and extended disordered domains [71]. Therefore, an alternative approach to inhibit the MYC activity is to target its binding partner, WDR5. For the inhibition assays, we employed BLI to test the efficacy of potential inhibitors at the WBM site. First, we quantitatively assessed C12, a small-molecule inhibitor, for the perturbation of the MbIIIb-WDR5 interaction (6UOZ.pdb; Supplementary Fig. S2) [30]. Our results demonstrated a concentration-dependent reduction in BLI response (Fig. 7a–b). On the other hand, we observed a marked decrease in the formation of the R5P-WDR5 complex in the presence of an R5P derivative, as its concentration increased from 1 μM to 10 μM (Fig. 7c, Table 1; Supplementary Table S12). Notably, the inhibitory effect at 1 μM concentration was relatively insignificant, necessitating an order of magnitude higher concentration to achieve a substantial inhibition (Fig. 7d).

In Fig. 7b and d, the normalized BLI responses, R_{norm}, illuminate that C12 is a much more effective inhibitor for the MbIIIb-WDR5 complex at sub-micromolar concentrations than the R5P derivative for the R5P-WDR5 complex. R_{norm} was determined for the inhibitor concentrations used in this study. However, its value likely changes for the absolute minimum (R_{min}) attained during a dose-response experiment. Our findings reveal that the interaction between RbBP5 and WDR5 can be effectively inhibited using an optimized peptidomimetic inhibitor derived from the WBM motif of RbBP5. While these inhibitors demonstrate their blocking potential against WBM-mediated interactions, further chemical modifications are required to amplify their effectiveness in targeting WDR5 interactions with other endogenous ligands. For example, similar efforts have been made to design peptidomimetic inhibitors against the Win site of WDR5 [72].

3.7. Concluding remarks

This study utilized BLI and seFRET microscopy to investigate the WBM site-mediated MYC-WDR5 and RbBP5-WDR5 interactions. This work provides a detailed analysis of the apparent kinetics of these interactions using corresponding consensus peptide ligands in a cell-free environment. Interestingly, our findings reveal a significant quantitative and qualitative overlap in the interactions of WDR5 with MYC and RbBP5. These insights significantly impact future drug development endeavors targeting the MYC-WDR5 interaction. Moreover, we tackled the specific localization of WDR5 within the nucleus in the presence and absence of full-length binding proteins in living HeLa cells. Finally, our study highlights the potential of peptidomimetics and small-molecule inhibitors as promising routes in drug delivery pipelines against the WBM site. By improving the structure and properties of these peptides, it may be possible to develop highly effective inhibitors that substantially disrupt the MYC-WDR5 interaction.

CRediT authorship contribution statement

Mohammad Ahmad: Visualization, Validation, Methodology, Investigation, Formal analysis, Conceptualization, Writing – review & editing, Writing – original draft. **Ali Imran:** Validation, Methodology, Investigation, Formal analysis, Writing – original draft. **Liviu Movileanu:** Supervision, Funding acquisition, Writing – review & editing.

Declaration of competing interest

The authors declare no competing interests.

Data availability

Data will be made available on request.

Acknowledgments

We thank members of this laboratory for their comments on the manuscript and their technical assistance during the very early stage of this project. We also thank Jenny Ross for providing access to the spinning-disk confocal microscope and Yazheng Wang for the BLI experiment with the R5P_V377G mutant. We are indebted to Tom Duncan for help with initial BLI experiments and Michael Cosgrove for offering a plasmid containing a gene that encodes $WDR5^{23-334}$. The National Institute of General Medical Sciences (GM088403 (to L.M.) and GM151299 (to L.M.)) and National Institute of Biomedical Imaging and Bioengineering (EB033412 (to L.M.)) of the National Institutes of Health supported this work.

Appendix A. Supplementary data

This supporting information includes the following: AlphaFold2-predicted 3D-structure of the full-length MYC and RbBP5 proteins; Dock pose of the full-length MYC and WDR5 proteins as well as the full-length RbBP5 and WDR5 proteins; The BLI-determined apparent association and dissociation rate constants for all inspected interactions; List of non-covalent interactions at the RbBP5-WDR5 interface; Equilibrium dissociation constants of the MbIIIb-WDR5 and R5P-WDR5 interactions; Apparent rate constants of association and dissociation of the MbIIIb-WDR5 and R5P-WDR5 interactions; Apparent kinetic and equilibrium constants of the R5P-WDR5 interaction at various salt concentrations; Schematic of the constructs developed and utilized for the live-cell imaging; Images of HeLa cells depicting the localization of WDR5; Localization of WDR5 and H2A in HeLa cell's nucleus; Scatter plot and bar graph showing the degree of colocalization between MYC and WDR5 as well as between RbBP5 and WDR5; Scheme for the calculation of calibration coefficients; NFRET values for the MYC-WDR5 and RbBP5-WDR5 interactions; Crystal structure of WDR5 in complex with C12 compound; Impact of R5P sequence-based inhibitor on the R5P-WDR5 interaction. Supplementary data to this article can be found online at https://doi.org/10.1016/j.ijbiomac.2023.128969.

References

[1] R.C. Trievel, A. Shilatifard, WDR5, a complexed protein, Nat. Struct. Mol. Biol. 16 (7) (2009) 678–680.
[2] A.F. Bryan, J. Wang, G.C. Howard, A.D. Guarnaccia, C.M. Woodley, E.R. Aho, E. J. Rellinger, B.K. Matlock, D.K. Flaherty, S.L. Lorey, D.H. Chung, S.W. Fesik, Q. Liu, A.M. Weissmiller, W.P. Tansey, WDR5 is a conserved regulator of protein synthesis gene expression, Nucleic Acids Res. 48 (6) (2020) 2924–2941.
[3] C.J. Jeffery, Moonlighting proteins, Trends Biochem. Sci. 24 (1) (1999) 8–11.
[4] A.D. Guarnaccia, W.P. Tansey, Moonlighting with WDR5: a cellular multitasker, J. Clin. Med. 7 (2) (2018) 21.
[5] B.P. Jain, S. Pandey, WD40 repeat proteins: signalling scaffold with diverse functions, Protein J. 37 (5) (2018) 391–406.
[6] M. Schapira, M. Tyers, M. Torrent, C.H. Arrowsmith, WD40 repeat domain proteins: a novel target class? Nat. Rev. Drug Discov. 16 (11) (2017) 773–786.
[7] C. Xu, J. Min, Structure and function of WD40 domain proteins, Protein Cell 2 (3) (2011) 202–214.
[8] C.U. Stirnimann, E. Petsalaki, R.B. Russell, C.W. Müller, WD40 proteins propel cellular networks, Trends Biochem. Sci. 35 (10) (2010) 565–574.
[9] B.D. Crawford, J.L. Hess, MLL core components give the green light to histone methylation, ACS Chem. Biol. 1 (8) (2006) 495–498.
[10] M.S. Cosgrove, A. Patel, Mixed lineage leukemia: a structure-function perspective of the MLL1 protein, FEBS J. 277 (8) (2010) 1832–1842.
[11] Y. Li, J. Han, Y. Zhang, F. Cao, Z. Liu, S. Li, J. Wu, C. Hu, Y. Wang, J. Shuai, J. Chen, L. Cao, D. Li, P. Shi, C. Tian, J. Zhang, Y. Dou, G. Li, Y. Chen, M. Lei, Structural basis for activity regulation of MLL family methyltransferases, Nature 530 (7591) (2016) 447–452.
[12] M. Vedadi, L. Blazer, M.S. Eram, D. Barsyte-Lovejoy, C.H. Arrowsmith, T. Hajian, Targeting human SET1/MLL family of proteins, Protein Sci. 26 (4) (2017) 662–676.
[13] H. Xue, T. Yao, M. Cao, G. Zhu, Y. Li, G. Yuan, Y. Chen, M. Lei, J. Huang, Structural basis of nucleosome recognition and modification by MLL methyltransferases, Nature 573 (7774) (2019) 445–449.
[14] H. Jiang, The complex activities of the SET1/MLL complex core subunits in development and disease, Biochim. Biophys. Acta. Gene. Regul. Mech. 1863 (7) (2020), 194560.
[15] L. Sha, A. Ayoub, U.S. Cho, Y. Dou, Insights on the regulation of the MLL/SET1 family histone methyltransferases, Biochim. Biophys. Acta Gene. Regul. Mech. 1863 (7) (2020), 194561.
[16] Y. Dou, T.A. Milne, A.J. Ruthenburg, S. Lee, J.W. Lee, G.L. Verdine, C.D. Allis, R. G. Roeder, Regulation of MLL1 H3K4 methyltransferase activity by its core components, Nat. Struct. Mol. Biol. 13 (8) (2006) 713–719.
[17] V. Dharmarajan, J.H. Lee, A. Patel, D.G. Skalnik, M.S. Cosgrove, Structural basis for WDR5 interaction (Win) motif recognition in human SET1 family histone methyltransferases, J. Biol. Chem. 287 (33) (2012) 27275–27289.
[18] S.A. Shinsky, M.S. Cosgrove, Unique role of the WD-40 repeat protein 5 (WDR5) subunit within the mixed lineage leukemia 3 (MLL3) histone methyltransferase complex, J. Biol. Chem. 290 (43) (2015) 25819–25833.
[19] Y.S. Ang, S.Y. Tsai, D.F. Lee, J. Monk, J. Su, K. Ratnakumar, J. Ding, Y. Ge, H. Darr, B. Chang, J. Wang, M. Rendl, E. Bernstein, C. Schaniel, I.R. Lemischka, Wdr5 mediates self-renewal and reprogramming via the embryonic stem cell core transcriptional network, Cell 145 (2) (2011) 183–197.
[20] K. Mitchell, S.A. Sprowls, S. Arora, S. Shakya, D.J. Silver, C.M. Goins, L. Wallace, G. Roversi, R.E. Schafer, K. Kay, T.E. Miller, A. Lauko, J. Bassett, A. Kashyap, J. D'Amato Kass, E.E. Mulkearns-Hubert, S. Johnson, J. Alvarado, J.N. Rich, E. C. Holland, P.J. Paddison, A.P. Patel, S.R. Stauffer, C.G. Hubert, J.D. Lathia, WDR5 represents a therapeutically exploitable target for cancer stem cells in glioblastoma, Genes Dev. 37 (3–4) (2023) 86–102.
[21] M.Z. Wu, Y.P. Tsai, M.H. Yang, C.H. Huang, S.Y. Chang, C.C. Chang, S.C. Teng, K. J. Wu, Interplay between HDAC3 and WDR5 is essential for hypoxia-induced epithelial-mesenchymal transition, Mol. Cell 43 (5) (2011) 811–822.
[22] C. Zhang, S. Ge, W. Gong, J. Xu, Z. Guo, Z. Liu, X. Gao, X. Wei, S. Ge, LncRNA ANRIL acts as a modular scaffold of WDR5 and HDAC3 complexes and promotes alteration of the vascular smooth muscle cell phenotype, Cell Death Dis. 11 (6) (2020) 435.
[23] A. Imran, B.S. Moyer, A.J. Canning, D. Kalina, T.M. Duncan, K.J. Moody, A. J. Wolfe, M.S. Cosgrove, L. Movileanu, Kinetics of the multitasking high-affinity Win binding site of WDR5 in restricted and unrestricted conditions, Biochem. J. 478 (11) (2021) 2145–2161.
[24] A. Imran, B.S. Moyer, D. Kalina, T.M. Duncan, K.J. Moody, A.J. Wolfe, M. S. Cosgrove, L. Movileanu, Convergent alterations of a protein hub produce divergent effects within a binding site, ACS Chem. Biol. 17 (6) (2022) 1586–1597.
[25] A. Imran, B.S. Moyer, A.J. Wolfe, M.S. Cosgrove, D.E. Makarov, L. Movileanu, Interplay of affinity and surface tethering in protein recognition, J. Phys. Chem. Lett. 13 (18) (2022) 4021–4028.
[26] A.D. Guarnaccia, K.L. Rose, J. Wang, B. Zhao, T.M. Popay, C.E. Wang, K. Guerrazzi, S. Hill, C.M. Woodley, T.J. Hansen, S.L. Lorey, J.G. Shaw, W.G. Payne, A. M. Weissmiller, E.T. Olejniczak, S.W. Fesik, Q. Liu, W.P. Tansey, Impact of WIN site inhibitor on the WDR5 interactome, Cell Rep. 34 (3) (2021), 108636.
[27] Y.W. Yang, R.A. Flynn, Y. Chen, K. Qu, B. Wan, K.C. Wang, M. Lei, H.Y. Chang, Essential role of lncRNA binding for WDR5 maintenance of active chromatin and embryonic stem cell pluripotency, Elife 3 (2014), e02046.
[28] F. Grebien, M. Vedadi, M. Getlik, R. Giambruno, A. Grover, R. Avellino, A. Skucha, S. Vittori, E. Kuznetsova, D. Smil, D. Barsyte-Lovejoy, F. Li, G. Poda, M. Schapira, H. Wu, A. Dong, G. Senisterra, A. Stukalov, K.V.M. Huber, A. Schönegger, R. Marcellus, M. Bilban, C. Bock, P.J. Brown, J. Zuber, K.L. Bennett, R. Al-Awar, R. Delwel, C. Nerlov, C.H. Arrowsmith, G. Superti-Furga, Pharmacological targeting of the Wdr5-MLL interaction in C/EBPα N-terminal leukemia, Nat. Chem. Biol. 11 (8) (2015) 571–578.
[29] J.D. Macdonald, S. Chacón Simon, C. Han, F. Wang, J.G. Shaw, J.E. Howes, J. Sai, J.P. Yuh, D. Camper, B.M. Alicie, J. Alvarado, S. Nikhar, W. Payne, E.R. Aho, J. A. Bauer, B. Zhao, J. Phan, L.R. Thomas, O.W. Rossanese, W.P. Tansey, A. G. Waterson, S.R. Stauffer, S.W. Fesik, Discovery and optimization of salicylic acid-derived sulfonamide inhibitors of the WD repeat-containing protein 5-MYC protein-protein interaction, J. Med. Chem. 62 (24) (2019) 11232–11259.
[30] S. Chacón Simon, F. Wang, L.R. Thomas, J. Phan, B. Zhao, E.T. Olejniczak, J. D. Macdonald, J.G. Shaw, C. Schlund, W. Payne, J. Creighton, S.R. Stauffer, A. G. Waterson, W.P. Tansey, S.W. Fesik, Discovery of WD repeat-containing protein 5 (WDR5)-MYC inhibitors using fragment-based methods and structure-based design, J. Med. Chem. 63 (8) (2020) 4315–4333.
[31] X. Chen, W. Xie, P. Gu, Q. Cai, B. Wang, Y. Xie, W. Dong, W. He, G. Zhong, T. Lin, J. Huang, Upregulated WDR5 promotes proliferation, self-renewal and chemoresistance in bladder cancer via mediating H3K4 trimethylation, Sci. Rep. 5 (2015) 8293.
[32] X. Chen, P. Gu, K. Li, W. Xie, C. Chen, T. Lin, J. Huang, Gene expression profiling of WDR5 regulated genes in bladder cancer, Genom. Data 5 (2015) 27–29.
[33] Z. Cui, H. Li, F. Liang, C. Mu, Y. Mu, X. Zhang, J. Liu, Effect of high WDR5 expression on the hepatocellular carcinoma prognosis, Oncol. Lett. 15 (5) (2018) 7864–7870.
[34] Y. Wu, P. Diao, Z. Li, W. Zhang, D. Wang, Y. Wang, J. Cheng, Overexpression of WD repeat domain 5 associates with aggressive clinicopathological features and unfavorable prognosis in head neck squamous cell carcinoma, J. Oral Pathol. Med. 47 (5) (2018) 502–510.
[35] G. Senisterra, H. Wu, A. Allali-Hassani, G.A. Wasney, D. Barsyte-Lovejoy, L. Dombrovski, A. Dong, K.T. Nguyen, D. Smil, Y. Bolshan, T. Hajian, H. He, A. Seitova, I. Chau, F. Li, G. Poda, J.F. Couture, P.J. Brown, R. Al-Awar, M. Schapira, C.H. Arrowsmith, M. Vedadi, Small-molecule inhibition of MLL activity by disruption of its interaction with WDR5, Biochem. J. 449 (1) (2013) 151–159.
[36] M. Schapira, C.H. Arrowsmith, Methyltransferase inhibitors for modulation of the epigenome and beyond, Curr. Opin. Chem. Biol. 33 (2016) 81–87.
[37] T.L. Downing, J. Soto, C. Morez, T. Houssin, A. Fritz, F. Yuan, J. Chu, S. Patel, D. V. Schaffer, S. Li, Biophysical regulation of epigenetic state and cell reprogramming, Nat. Mater. 12 (12) (2013) 1154–1162.
[38] P. Wang, M. Dreger, E. Madrazo, C.J. Williams, R. Samaniego, N.W. Hodson, F. Monroy, E. Baena, P. Sánchez-Mateos, A. Hurlstone, J. Redondo-Muñoz, WDR5 modulates cell motility and morphology and controls nuclear changes induced by a 3D environment, Proc. Natl. Acad. Sci. U. S. A. 115 (34) (2018) 8581–8586.
[39] A. Patel, V. Dharmarajan, M.S. Cosgrove, Structure of WDR5 bound to mixed lineage leukemia protein-1 peptide, J. Biol. Chem. 283 (47) (2008) 32158–32161.
[40] P. Zhang, H. Lee, J.S. Brunzelle, J.F. Couture, The plasticity of WDR5 peptide-binding cleft enables the binding of the SET1 family of histone methyltransferases, Nucleic Acids Res. 40 (9) (2012) 4237–4246.
[41] M. Ahmad, J.H. Ha, L.A. Mayse, M.F. Presti, A.J. Wolfe, K.J. Moody, S.N. Loh, L. Movileanu, A generalizable nanopore sensor for highly specific protein detection at single-molecule precision, Nat. Commun. 14 (1) (2023) 1374.
[42] Z. Odho, S.M. Southall, J.R. Wilson, Characterization of a novel WDR5-binding site that recruits RbBP5 through a conserved motif to enhance methylation of histone H3 lysine 4 by mixed lineage leukemia protein-1, J. Biol. Chem. 285 (43) (2010) 32967–32976.
[43] J.J. Song, R.E. Kingston, WDR5 interacts with mixed lineage leukemia (MLL) protein via the histone H3-binding pocket, J. Biol. Chem. 283 (50) (2008) 35258–35264.
[44] A. Patel, V.E. Vought, V. Dharmarajan, M.S. Cosgrove, A conserved arginine-containing motif crucial for the assembly and enzymatic activity of the mixed lineage leukemia protein-1 core complex, J. Biol. Chem. 283 (47) (2008) 32162–32175.
[45] L.R. Thomas, Q. Wang, B.C. Grieb, J. Phan, A.M. Foshage, Q. Sun, E.T. Olejniczak, T. Clark, S. Dey, S. Lorey, B. Alicie, G.C. Howard, B. Cawthon, K.C. Ess, C. M. Eischen, Z. Zhao, S.W. Fesik, W.P. Tansey, Interaction with WDR5 promotes target gene recognition and tumorigenesis by MYC, Mol. Cell. Biochem. 58 (3) (2015) 440–452.
[46] A. Ali, S. Tyagi, Diverse roles of WDR5-RbBP5-ASH2L-DPY30 (WRAD) complex in the functions of the SET1 histone methyltransferase family, J. Biosci. 42 (1) (2017) 155–159.
[47] C.Y. Lin, J. Lovén, P.B. Rahl, R.M. Paranal, C.B. Burge, J.E. Bradner, T.I. Lee, R. A. Young, Transcriptional amplification in tumor cells with elevated c-Myc, Cell 151 (1) (2012) 56–67.
[48] M.J. Duffy, S. O'Grady, M. Tang, J. Crown, MYC as a target for cancer treatment, Cancer Treat. Rev. 94 (2021), 102154.
[49] L.R. Thomas, C.M. Adams, J. Wang, A.M. Weissmiller, J. Creighton, S.L. Lorey, Q. Liu, S.W. Fesik, C.M. Eischen, W.P. Tansey, Interaction of the oncoprotein transcription factor MYC with its chromatin cofactor WDR5 is essential for tumor maintenance, Proc. Natl. Acad. Sci. U. S. A. 116 (50) (2019) 25260–25268.
[50] C.J. Weeramange, M.S. Fairlamb, D. Singh, A.W. Fenton, L. Swint-Kruse, The strengths and limitations of using biolayer interferometry to monitor equilibrium titrations of biomolecules, Protein Sci. 29 (4) (2020) 1018–1034.
[51] W.R. Algar, N. Hildebrandt, S.S. Vogel, I.L. Medintz, FRET as a biomolecular research tool - understanding its potential while avoiding pitfalls, Nat. Methods 16 (9) (2019) 815–829.
[52] M. Ahmad, L. Movileanu, Multiplexed imaging for probing RAS-RAF interactions in living cells, Biochim. Biophys. Acta Biomembr. 1865 (6) (2023), 184173.

[53] J. Jumper, R. Evans, A. Pritzel, T. Green, M. Figurnov, O. Ronneberger, K. Tunyasuvunakool, R. Bates, A. Žídek, A. Potapenko, A. Bridgland, C. Meyer, S.A. A. Kohl, A.J. Ballard, A. Cowie, B. Romera-Paredes, S. Nikolov, R. Jain, J. Adler, T. Back, S. Petersen, D. Reiman, E. Clancy, M. Zielinski, M. Steinegger, M. Pacholska, T. Berghammer, S. Bodenstein, D. Silver, O. Vinyals, A.W. Senior, K. Kavukcuoglu, P. Kohli, D. Hassabis, Highly accurate protein structure prediction with AlphaFold, Nature 596 (7873) (2021) 583–589.
[54] K. Tunyasuvunakool, J. Adler, Z. Wu, T. Green, M. Zielinski, A. Žídek, A. Bridgland, A. Cowie, C. Meyer, A. Laydon, S. Velankar, G.J. Kleywegt, A. Bateman, R. Evans, A. Pritzel, M. Figurnov, O. Ronneberger, R. Bates, S.A.A. Kohl, A. Potapenko, A. J. Ballard, B. Romera-Paredes, S. Nikolov, R. Jain, E. Clancy, D. Reiman, S. Petersen, A.W. Senior, K. Kavukcuoglu, E. Birney, P. Kohli, J. Jumper, D. Hassabis, Highly accurate protein structure prediction for the human proteome, Nature 596 (7873) (2021) 590–596.
[55] M. AlQuraishi, Machine learning in protein structure prediction, Curr. Opin. Chem. Biol. 65 (2021) 1–8.
[56] G.C.P. van Zundert, J. Rodrigues, M. Trellet, C. Schmitz, P.L. Kastritis, E. Karaca, A. S.J. Melquiond, M. van Dijk, S.J. de Vries, A. Bonvin, The HADDOCK2.2 web server: user-friendly integrative modeling of biomolecular complexes, J. Mol. Biol. 428 (4) (2016) 720–725.
[57] B. Moser, B. Hochreiter, R. Herbst, J.A. Schmid, Fluorescence colocalization microscopy analysis can be improved by combining object-recognition with pixel-intensity-correlation, Biotechnol. J. 12 (1) (2017), 1600332.
[58] A.H. Clayton, A. Chattopadhyay, Taking care of bystander FRET in a crowded cell membrane environment, Biophys. J. 106 (6) (2014) 1227–1228.
[59] Z. Xia, Y. Liu, Reliable and global measurement of fluorescence resonance energy transfer using fluorescence microscopes, Biophys. J. 81 (4) (2001) 2395–2402.
[60] L.A. Mayse, A. Imran, Y. Wang, M. Ahmad, R.A. Oot, S. Wilkens, L. Movileanu, Evaluation of nanopore sensor design using electrical and optical analyses, ACS Nano 17 (11) (2023) 10857–10871.
[61] L.A. Mayse, A. Imran, M.G. Larimi, M.S. Cosgrove, A.J. Wolfe, L. Movileanu, Disentangling the recognition complexity of a protein hub using a nanopore, Nat. Commun. 13 (1) (2022) 978.
[62] G. Schreiber, G. Haran, H.X. Zhou, Fundamental aspects of protein-protein association kinetics, Chem. Rev. 109 (3) (2009) 839–860.
[63] R.A. Curtis, J. Ulrich, A. Montaser, J.M. Prausnitz, H.W. Blanch, Protein-protein interactions in concentrated electrolyte solutions, Biotechnol. Bioeng. 79 (4) (2002) 367–380.
[64] T. Nagai, K. Ibata, E.S. Park, M. Kubota, K. Mikoshiba, A. Miyawaki, A variant of yellow fluorescent protein with fast and efficient maturation for cell-biological applications, Nat. Biotechnol. 20 (1) (2002) 87–90.
[65] G.J. Kremers, J. Goedhart, E.B. van Munster, T.W. Gadella Jr., Cyan and yellow super fluorescent proteins with improved brightness, protein folding, and FRET Förster radius, Biochemistry 45 (21) (2006) 6570–6580.
[66] D.S. Bindels, L. Haarbosch, L. van Weeren, M. Postma, K.E. Wiese, M. Mastop, S. Aumonier, G. Gotthard, A. Royant, M.A. Hink, T.W. Gadella Jr., mScarlet: a bright monomeric red fluorescent protein for cellular imaging, Nat. Methods 14 (1) (2017) 53–56.
[67] T. Wang, K. Birsoy, N.W. Hughes, K.M. Krupczak, Y. Post, J.J. Wei, E.S. Lander, D. M. Sabatini, Identification and characterization of essential genes in the human genome, Science 350 (6264) (2015) 1096–1101.
[68] H.A. Benink, M. Urh, HaloTag technology for specific and covalent labeling of fusion proteins, Methods Mol. Biol. 1266 (2015) 119–128.
[69] F.V. Subach, G.H. Patterson, M. Renz, J. Lippincott-Schwartz, V.V. Verkhusha, Bright monomeric photoactivatable red fluorescent protein for two-color super-resolution sptPALM of live cells, J. Am. Chem. Soc. 132 (18) (2010) 6481–6491.
[70] L.R. Thomas, A.M. Foshage, A.M. Weissmiller, W.P. Tansey, The MYC-WDR5 nexus and cancer, Cancer Res. 75 (19) (2015) 4012–4015.
[71] E. Wolf, M. Eilers, Targeting MYC proteins for tumor therapy, Ann. Rev. Cancer Biol. 4 (2020) 61–75.
[72] N.L. Alicea-Velázquez, S.A. Shinsky, D.M. Loh, J.H. Lee, D.G. Skalnik, M. S. Cosgrove, Targeted disruption of the interaction between WD-40 repeat protein 5 (WDR5) and mixed lineage leukemia (MLL)/SET1 family proteins specifically inhibits MLL1 and SETd1A methyltransferase complexes, J. Biol. Chem. 291 (43) (2016) 22357–22372.
[73] G.P. Quinn, M.J. Keough, Experimental Design and Data Analysis for Biologists, 6th ed., Cambridge University Press, Cambridge, UK, 2007.